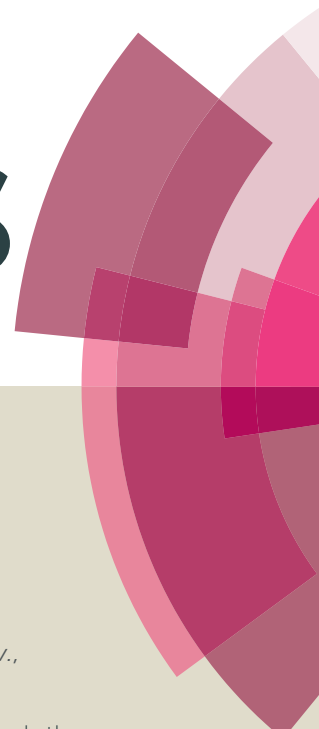


# RSC Advances



This article can be cited before page numbers have been issued, to do this please use: S. Panneri, N. Kumar, N. Madhavan, D. Kumar, B. N. Nair, A. M. Peer, K. G. K. Warriar and H. U. N. Saraswathy, *RSC Adv.*, 2015, DOI: 10.1039/C5RA13316E.



This is an *Accepted Manuscript*, which has been through the Royal Society of Chemistry peer review process and has been accepted for publication.

*Accepted Manuscripts* are published online shortly after acceptance, before technical editing, formatting and proof reading. Using this free service, authors can make their results available to the community, in citable form, before we publish the edited article. This *Accepted Manuscript* will be replaced by the edited, formatted and paginated article as soon as this is available.

You can find more information about *Accepted Manuscripts* in the [Information for Authors](#).

Please note that technical editing may introduce minor changes to the text and/or graphics, which may alter content. The journal's standard [Terms & Conditions](#) and the [Ethical guidelines](#) still apply. In no event shall the Royal Society of Chemistry be held responsible for any errors or omissions in this *Accepted Manuscript* or any consequences arising from the use of any information it contains.

## Reactive Oxygen Species (ROS) Mediated Enhanced Anti-candidal Activity of ZnS-ZnO Nanocomposites with Low Inhibitory Concentrations

P. Suyana<sup>a</sup>, S. NishanthKumar<sup>b</sup>, NimishaMadhavan<sup>a</sup>, B. S. DileepKumar<sup>b,d</sup>, Balagopal N. Nair<sup>c</sup>, A. Peer Mohamed<sup>a</sup>, K. G. K. Warriar<sup>a,d</sup> and U. S. Hareesh<sup>a,d\*</sup>

<sup>a</sup>Material Science and Technology Division

<sup>b</sup>Agroprocessing and Natural Products Division

National Institute for Interdisciplinary Science and Technology (CSIR-NIIST)

Thiruvananthapuram-695019, India

<sup>c</sup>R& D Centre, Noritake Co. Limited, Aichi 470-0293, Japan

<sup>d</sup>Academy of Scientific and Innovative Research, New Delhi, India

\*Corresponding author E-mail: [hareesh@niist.res.in](mailto:hareesh@niist.res.in)

Telephone: 0091 4712535504

Fax: 0091 471 2491712

---

### Abstract

Enhanced antifungal activity against the yeast species of *Candida albicans*, *Candida tropicalis* and *Saccharomyces cerevisiae* was displayed by ZnS-ZnO nanocomposites prepared by a simple precipitation technique. The antifungal activity was significantly more in the presence of indoor light than under dark conditions and was a clear confirmation of the inhibitory role of reactive oxygen species (ROS) generated *insitu* by the photocatalytic nanocomposites. The generation of ROS was further evidenced by flow cytometry results and membrane permeabilisation studies. Time kill assay and growth curve analysis indicated diminished antifungal activity under dark conditions due primarily to Zn<sup>2+</sup> efflux in solution.

## Introduction

Semiconductor nanoparticles are employed in recent years as an environmentally benign solution for pollution control as well as for the disinfection of harmful microbes like *Escherichia coli*, *Staphylococcus aureus*, and *Candida albicans*.<sup>1-7</sup> Advanced oxidation process based on semiconductor mediated photocatalytic degradation of the pollutants and microbes is the primary mechanism underlying this technique.<sup>8-9</sup> Unlike other methods, photocatalytic disinfection or degradation is simple, cost effective, and safe as only light is needed as energy source and no harmful by-products are released.<sup>10-11</sup> Semiconductors like TiO<sub>2</sub>, ZnO, ZnS, etc are proven to be effective materials for the photocatalytic degradation of the organic compounds and disinfection of microbes.<sup>12-19</sup>

ZnS is an important semiconductor whose theoretical photocarrier efficiency is much higher than TiO<sub>2</sub>.<sup>20</sup> It is one of the first semiconductors invented and has wide range of applications in electronic, optical, biomedical, and photovoltaic devices. The unique size dependent properties ZnS nanoparticles enable its wide spread applications in solar cells, LEDs, catalysis, and as sensors and antimicrobial agents. Due to its high energy conversion efficiency and the relatively negative redox potential of conduction band, it has been well suited for application as a photocatalyst.<sup>21-22</sup> However, owing to its large bandgap, ZnS is active only in the UV region and more efficient visible light harvesting would render this material quite attractive for practical applications in the area of photocatalysis and photovoltaics.

A simple and cost effective strategy to improve the activity of ZnS is to develop nanocomposites with compatible semiconductors. The synergistic effects of individual semiconductors could lead to more effective electron-hole pair separation by retarding the recombination process.<sup>23-</sup>

<sup>24</sup> Among these, ZnS–ZnO nanocomposites is a priority choice by virtue of its lower photoexcitation threshold energy and improved electron transfer paths than the individual components. <sup>25</sup> The large difference in electronegativity values and sizes between S and O modify the electrical and optical properties of ZnS-ZnO combinations. <sup>26-27</sup> The nanocomposites thus promote the electron transfer process with photogenerated electrons flowing from ZnS to ZnO. <sup>22</sup> The recombination rate of the charge carriers thus decrease immensely as a result of their physically separated band gap. Till date, many experimental methodologies are reported for the effective synthesis of ZnS-ZnO composites. <sup>28-32</sup> Most of the available reports are focused on development of heterostructured 1D ZnO/ZnS nanowires, nanoribbons, nanocables or nanobelts for various applications like electricity generation, luminescent applications, sensors, optoelectronic devices etc. However the preparation methods require sophisticated conditions to obtain the heterostructures. <sup>30, 32-35</sup>

In the present work a simple water based co-precipitation technique was employed for the synthesis of ZnS-ZnO nanocomposites. The prepared nanocomposites were tested for their antimicrobial activity against the important yeast species of *Candida albicans* (*C. albicans*), *Candida tropicalis* (*C. tropicalis*) and *Saccharomyces cerevisiae* (*S. cerevisiae*) and their minimum inhibitory concentrations were elucidated. To the best of our knowledge this is the first study employing ZnS-ZnO nanocomposites for antimicrobial applications. The generation and role of reactive oxygen species (ROS) in reducing the microbial burden was identified by flow cytometry measurements. Damage of cell membrane due to ROS was studied by cell permeabilisation studies using propidium iodide uptake assay. A systematic evaluation employing time kill assay and growth curves under light and dark conditions permitted comprehensive analysis of the inhibitory role of photo induced ROS in fungal growth.

## 2. Experimental

### 2.1. Synthesis of ZnS-ZnO nanocomposites

In a typical synthesis, aqueous solution of sodium hydroxide (1.0 M) was added drop by drop to an aqueous solution of zinc nitrate hexahydrate (0.5 M) and the mixture was stirred for 3 hours. The ZnO thus obtained was added drop wise to an aqueous solution of zinc acetate dihydrate (0.5 M) with constant stirring. An aqueous solution of sodium sulphide (0.5 M) was then added and stirring was continued for 1 hour. The thick white precipitate obtained was filtered, washed with distilled water, and dried at 100<sup>0</sup> C. Three different compositions of ZnS: ZnO containing 3:1, 1:1, and 1:3 weight ratios were prepared and are denoted as ZSO31, ZSO11, and ZSO13 respectively here after. Pure ZnS was prepared using zinc acetate and sodium sulphide through a simple precipitation method.

### 2.2. Characterization of photocatalyst

The prepared nanocomposites were characterized by X-ray diffraction (Philips X'pert Pro diffractometer) in the 2 $\theta$  range of 10–80<sup>0</sup> using Cu K $\alpha$  radiation to evaluate the crystal structure and purity. BET surface area measurements were carried out using a BET surface area analyser (Gemini 2375, Micromeritics, USA) after degassing the samples at 200<sup>0</sup>C for 2 hours. SEM images were acquired on an EVO 18Special Edition scanning electron microscope (Carl Zeiss, Germany) operating at 20 kV. The morphology of the nanocrystallites was observed through a high resolution transmission electron microscope (HRTEM, FEI Tecnai 30 G<sup>2</sup>S-TWIN) operated at an accelerating voltage of 300 kV. The diffused reflectance spectra of the prepared materials were analyzed using a spectrophotometer in the spectral band width of 200–800 nm (Shimadzu UV 2401 PC).

## 2.3. Antimicrobial study

### 2.3.1. Growth condition and maintenance of test organisms

The test yeast strains used in the study were *Candida albicans* MTCC 277, *Candida tropicalis* MTCC 184, and *Saccharomyces cerevisiae* MTCC 463 procured from the Microbial Type Culture Collection and Gene Bank (MTCC) Division, CSIR-Institute of Microbial Technology (IMTECH), Chandigarh, India. Stock culture was maintained on slants of PD agar (containing dextrose 40 g l<sup>-1</sup>, peptone 10 g l<sup>-1</sup> and agar 15 g l<sup>-1</sup>) at 4°C. The primary culture of the yeast species was prepared from the stock slant into the PD broth medium and incubated at 30°C for 48 h (stationary phase, 10<sup>8</sup> CFU/ml). The primary culture (1 ml) was re-inoculated into the 50 ml fresh PD broth and grown for 12 h up to mid-log phase (approx. 10<sup>5</sup> CFU/ml) at 30°C. All experiments were performed from the mid-log phase (10<sup>5</sup> CFU/ml) freshly grown yeast spp. culture in triplicates.

### 2.3.2. Minimum inhibition concentration (MIC)

The MIC is the lowest concentration at which a material exhibits antimicrobial activity and this was done by serial dilution technique according Clinical and Laboratory standard Institute (CLSI). Sterile test tubes were taken separately with 9.9 ml of saline water, inoculated with 10<sup>5</sup> CFU/ml of corresponding microorganisms. To this, different concentrations (2–500 mg/ml) of ZSO31, ZSO11, and ZSO13 were added to individual test tubes. The whole setup was allowed to grow overnight at for 48 h. Negative and positive control tubes contained only inoculated broth and free nanoparticles suspension. Compounds were tested three times and the results were averaged. The visual turbidity of the tubes was noted before and after incubation. The MIC was estimated as lowest concentration of the nanoparticles that did not permit any visible growth of microbes during 24 h of incubation on the basis of turbidity. To avoid the possibility of

misinterpretations due to the turbidity of insoluble compounds, if any, the MIC was determined by subculturing the above serial dilutions after 24 h and plated in PD agar.

### 2.3.3 Effect of nanoparticles on yeast spp. by studying the Growth kinetics

Yeast spp. was cultured on PD agar plates for 18 h at 30°C before use. MIC concentrations of ZnO, ZnS, ZSO31, ZSO11 and ZSO13 nanoparticles were prepared in sterilized PD medium to a final volume of 10 ml. A single colony of each yeast spp. was used for inoculating the PDB medium containing the nanoparticles as well as a positive control containing only yeast spp. (without any nanoparticles). Aliquots were taken from 0, 1, 2, 4, 6, 12, 24, and 48 h for measurement of the optical density at 600 nm. The plates were incubated at 30°C for 48 h. The light source used was a normal household fluorescent lamp. All the experiments under dark were conducted using the suspensions prepared in the dark and culture grown in dark conditions by the culture tubes with aluminum foil.

### 2.3.4 Time–kill curve analysis

A time–kill curve (CFU as a function of time) was evaluated to study the rate and extent of reduction in *Candidal* burden when treated with MIC concentration of nanoparticles (ZnO, ZnS, ZSO31, ZSO11, and ZSO13). The experiments were conducted in PDB for 48 h. The concentrations used were the MIC values of corresponding nanoparticles. An initial inoculum of approximately  $1 \times 10^6$  CFU/ml was taken for all the experiments. Samples (0.1 ml) were collected at 0, 2, 4, 6, 8, 12, 24, and 48 h and serially diluted in normal saline and aliquoted in onto PDA. These plates were then incubated at 30°C for 48 h and the colonies were counted. The broth without any agent was used as the control. The data were plotted as log CFU/ml versus time (h) for each time point. Tests were performed three times. Significant activity was defined

as a decrease of  $\geq 2 \log_{10}$  CFU/ml after 48 h. Lowest limit of quantification of time kill assay was  $1 \log_{10}$  CFU/ml (99.99 % reduction).

### 2.3.5 Estimation of Intracellular Reactive Oxygen Species (ROS) by flow cytometry analysis

For the detection of reactive oxygen species (ROS) produced over a 4 h culture period after the treatment of MIC concentration of nanoparticles, cells were incubated with  $20 \mu\text{M}$  CM-H<sub>2</sub>DCFDA [5-(and-6)-chloromethyl-2',7'-dichlorodihydrofluoresceindiacetate acetyl ester] for 30 min in the dark at 35°C. The DCFH-DA passively enters the cell where it reacts with ROS to form highly fluorescent dichlorofluorescein (DCF). Then, the cells were harvested, washed, re-suspended in PBS, and immediately analyzed by flow cytometry (BD science). CM-H<sub>2</sub>DCFDA readily diffuses through the cell membrane and is hydrolyzed by intracellular esterases to non-fluorescent dichlorofluorescein (DCFH), which is then rapidly oxidized to highly fluorescent DCF (2',7'-dichlorofluorescein) as a result of a broad range of intracellular oxidative stresses other than H<sub>2</sub>O<sub>2</sub>. The fluorescence intensity of DCF is proportional to the intracellular amount of ROS formed<sup>36</sup>.

### 2.3.6 Membrane Permeabilisation studies due to ROS production

Permeabilisation of fungal membrane after the combination treatment was checked by using propidium iodide (PI), a membrane impermeable dye.<sup>37</sup> For this, actively growing *C. albicans* cells ( $\sim 1 \times 10^6$  CFU/ml) were suspended in an RPMI-1640 medium containing nanocomposites and PI ( $1.49 \mu\text{M}$ ). After incubation for 1 h at 30 °C with constant shaking (200 rpm), cells were harvested by centrifugation and suspended in phosphate buffer saline (PBS, pH 7.4). The cells were then visualized by confocal laser scanning microscopy (BD Pathway<sup>TM</sup>Bioimager System,

BD Biosciences) with a wavelength of 560 nm for PI. Cells without violacein and azoles served as controls.<sup>38</sup>

### 3 Results

X-ray diffraction, presented in Fig. 1, was used to analyze the crystal structure and phase purity of the prepared samples. The prepared ZnS crystallized in the cubic sphalerite form while the ZnO was obtained in hexagonal wurtzite structure. The ZnS particles were nanosized as indicated by broadened XRD peaks. The ZnO peaks were highly crystalline and narrow. The composites indicated peaks corresponding to both ZnS and ZnO. ZnO has three prominent peaks at  $2\theta = 31.7^\circ$ ,  $34.4^\circ$ , and  $36.3^\circ$  corresponding to (100), (002), and (101) planes respectively. ZnS has three peaks at  $28.8^\circ$ ,  $48^\circ$ , and  $56^\circ$  corresponding to (111), (220), and (311) planes. As the concentration of ZnO increased, the ZnS peak intensity was found reduced. No other impurities were present in the composites.

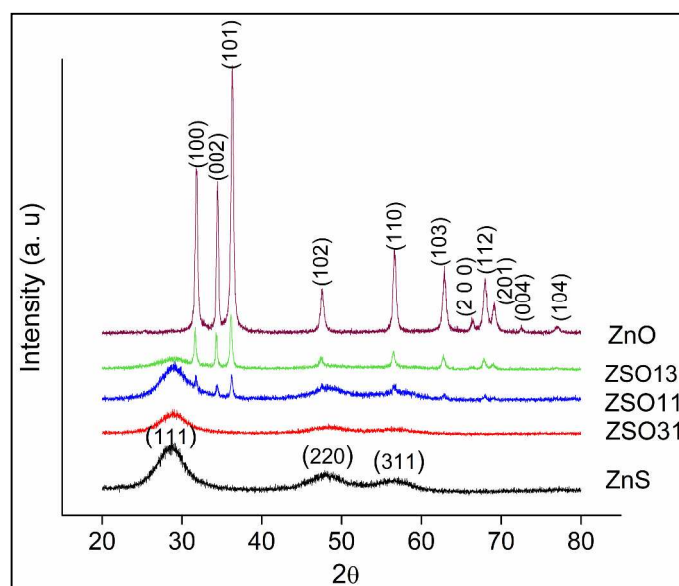


**Fig.1** X-ray diffraction pattern of ZnS, ZSO31, ZSO11, ZSO13, and ZnO

The transmission electron micrographs of the samples presented in Fig. 2 provided the morphological features of synthesized nano composites. Fig. 2a represented the ZnS nanoparticles obtained by the precipitation of zinc acetate using sodium sulphide. The individual particles were found extremely fine sized and uniform though they appeared agglomerated in the absence of any surface modification. The measurements done on the TEM image of ZnS nanoparticles provided particle size values under 5nm. On the contrary, the ZnO precipitation from zinc nitrate resulted in sub-micron sized particles of average size 0.4 microns with a morphology resembling that of rice grains (Fig 2b). The fine precipitates of ZnS were seen coated over the grain shaped ZnO particles in the ZSO31 nanocomposite presented in Fig. 2c. The surface coverage of ZnO by ZnS nanoparticles were observed also for the ZSO13 composition despite the significant increase in ZnO concentration. This was primarily ascribed to the high surface area of the synthesized ZnS particles compared to ZnO. The TEM studies have conclusively confirmed the composite microstructure as ZnS coated ZnO particles.

Figure 2B provides the EDAX pattern of the ZSO31 sample which clearly indicated that the particles are composed of the elements of Zn, S, and O only. This observation substantiated the XRD results on the phase composition of the ZSO31 sample. The morphology of ZnO particles were further confirmed from SEM micrographs presented in Figure 2C. As observed in TEM, the ZnO particles were of uniform size and of rice grain type morphology with an approximate length of 400 nm and diameter of 200 nm.

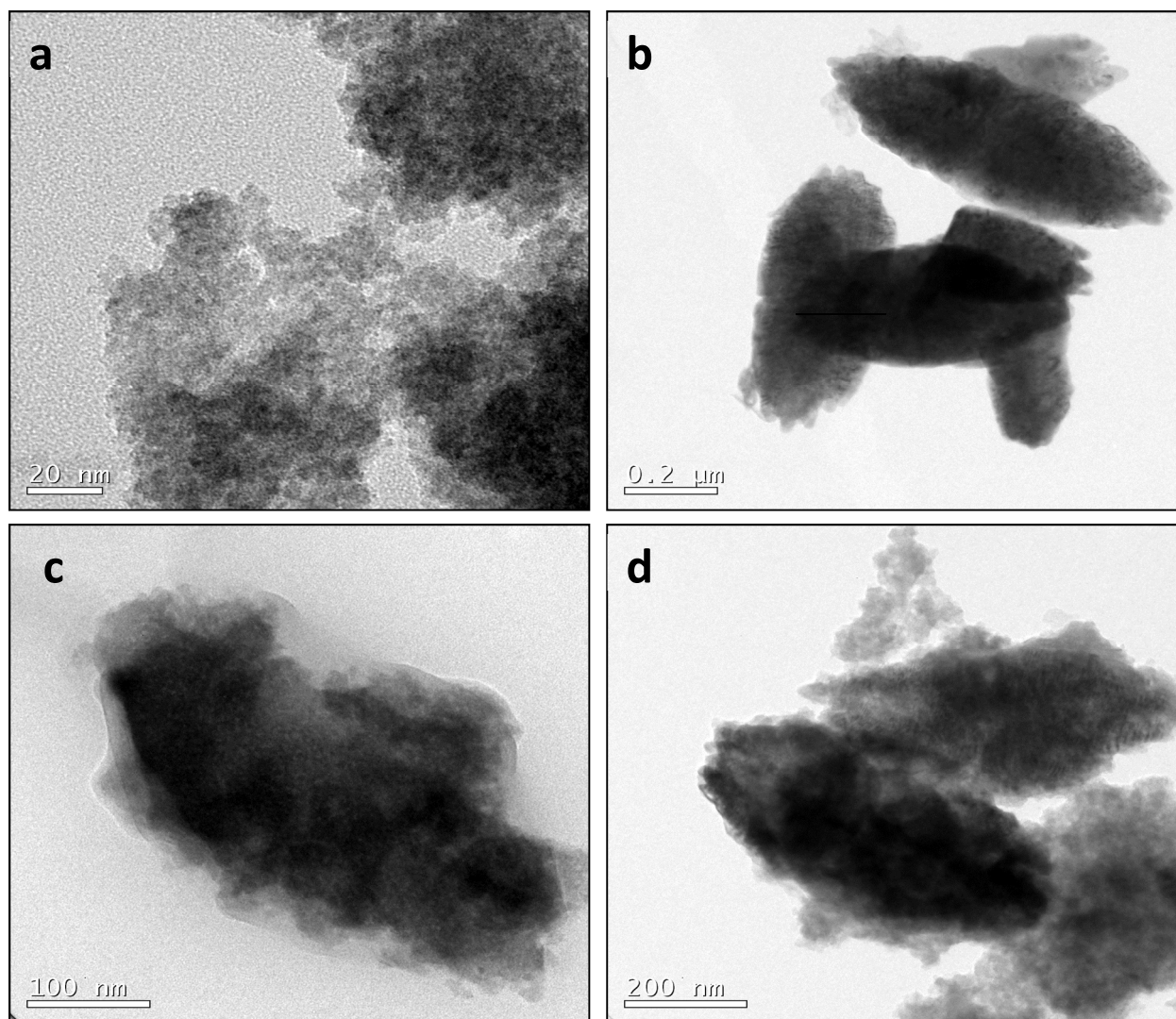


**Fig. 2A** TEM micrographs of a) ZnS, b) ZnO c) ZSO31 and d) ZSO13

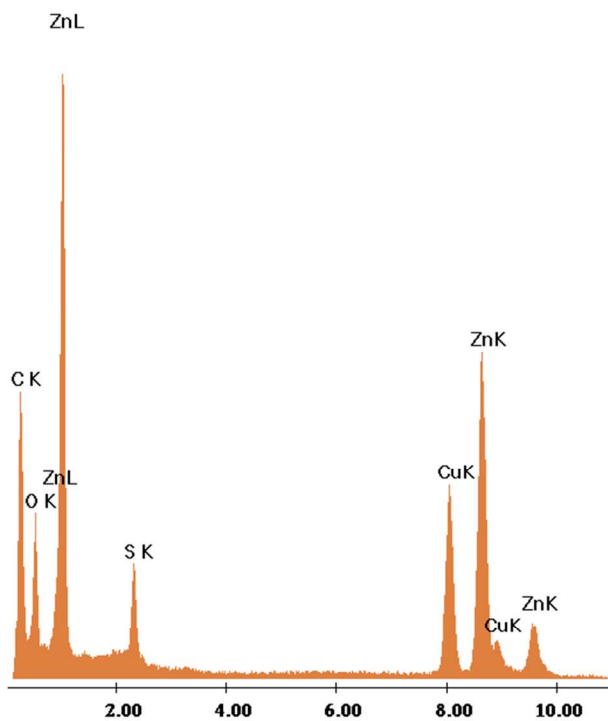


Fig. 2B EDAX spectrum of ZSO31

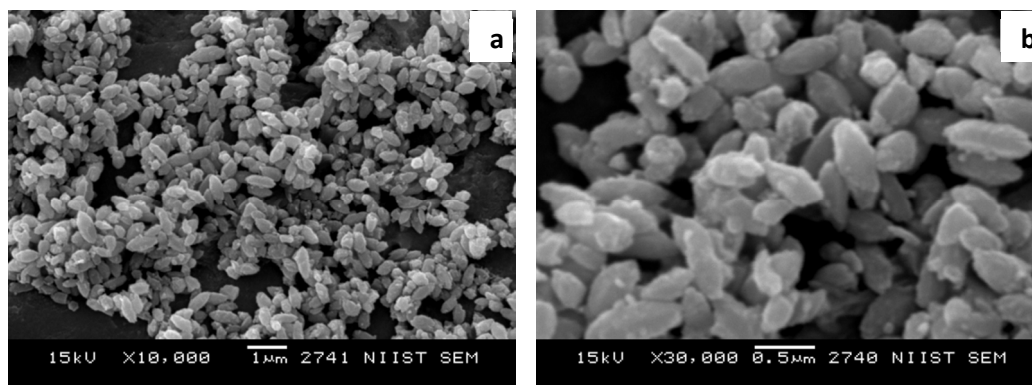
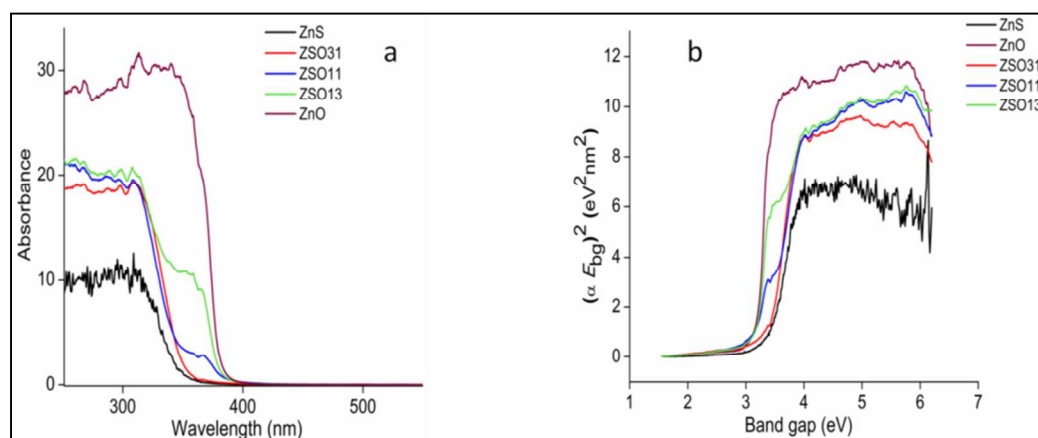


Fig. 2C SEM images of ZnO submicron particles at a) low b) high magnifications

The electronic properties of the prepared composite samples were analyzed by the diffused reflectance spectra provided in Fig. 3. The absorbance patterns of samples in the spectral region of 200-400 nm presented in Fig 3a indicated that the ZnSnano particles possessed an absorption edge at 346 nm and the ZnO particles at 382 nm. The nano composites with the three different weight proportions had values intermediate between the two pure samples of ZnO and ZnS. Addition of ZnO to ZnS shifted the absorbance to higher wavelength regions but within that observed for ZnO.



**Fig. 4** a. UV-Vis Absorption spectra and b. the corresponding band gap values of ZnS, ZSO31, ZSO11, ZSO13, and ZnO

Fig 3b presented the bang gap values estimated using the Tauc plot. The band gap of ZnS nanoparticles was calculated to be 3.3 eV and was found considerably less than the value of 3.6 reported for bulk ZnS. Sub-micron ZnO particles possessed  $E_g$  value of 3.0 and was in accordance with reported values. The band gap values of the ZnS-ZnO composites were found to

be in between that of ZnO and ZnS. The nanocomposite formation facilitated modification of band gap values and absorbance patterns. However, the modifications were not sufficient enough to extend the absorption characteristics to the visible light region.

**Table 1** BET Surface Area of samples of ZnS-ZnO nanocomposites and their individual constituents

Sample	Surface area $\text{m}^2/\text{g}$
ZnS	170
ZnO	2
ZSO31	168
ZSO 11	172
ZSO13	97

The surface area values of ZnS, ZnO and their composites presented in Table 1 indicated that the pure ZnS particles derived by the precipitation reaction yielded high surface area values of  $170 \text{ m}^2/\text{g}$  while the grain shaped ZnO particles possessed almost negligible surface area values of  $\sim 2 \text{ m}^2/\text{g}$ . The adsorption isotherms displayed a shape characteristic of surface adsorption in solids. The ZnS-ZnO compositions containing up to 50wt% ZnS indicated surface area (Table 1) values as high as that of pure ZnS particles. The adsorption isotherms presented in Fig. 4 indicated the porous nature of ZnS and ZnS rich composites (ZSO11 and ZSO31).

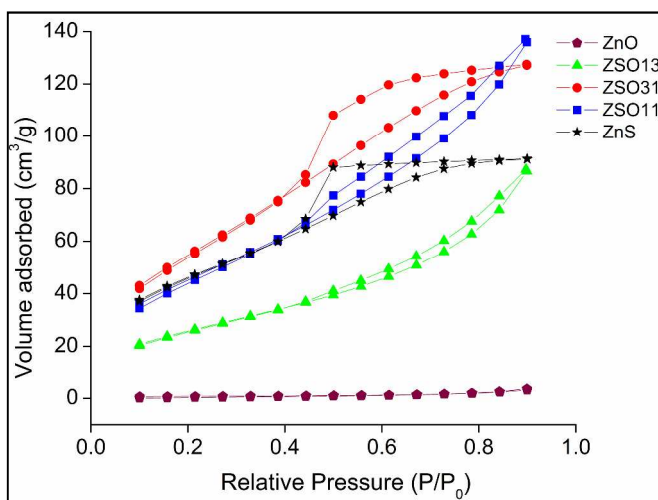


**Fig. 5 Nitrogen** adsorption-desorption isotherm of ZnS, ZSO31, ZSO11, ZSO13, and ZnO

From the shape of the isotherms and the adsorption values, it was safe to assume that the presence of low amounts of ZnO has helped to reduce the agglomeration of ZnS thus providing surface area values higher than the pure ZnS itself. However, as the ZnO concentration increased (ZSO13) the composite behaved more like ZnO with a coating of ZnS over it.

**3.1. Antifungal Activity**

The minimum inhibitory concentrations (MIC) of the nanocomposites in comparison with the individual constituents tabulated in Table 2 indicated that the MIC of ZnS: ZnO compositions in all the proportions studied were much less than that of pure ZnO. Of the compositions, ZnO was found to possess the highest MIC of 250  $\mu\text{g/ml}$  presumably due to its larger size and poor surface area. The ZnS nanoparticle displayed MIC value of 64  $\mu\text{g/ml}$  and was considerably lower than that of ZnO. Significant activity was recorded by ZSO31 compositions with MIC value as low as 16  $\mu\text{g/ml}$  against *C. albicans*.

**Table 2:** Minimum Inhibitory Concentrations (MIC) of samples

Photocatalyst	MIC ( $\mu\text{g/ml}$ )		
	<i>C. albicans</i>	<i>C. tropicalis</i>	<i>S. cerevisiae</i>
ZnO	250	500	1000
ZnS	64	64	500
ZSO31	16	32	64

ZSO11	32	64	125
ZSO13	64	64	125

### 3.2. Time kill assay

Time-kill assays for the nanoparticles, on the yeast species investigated, are shown in Fig. 6.

Figures 5 (a-f) represented the time-kill curves of nanoparticles with *C. albicans*, *C. tropicalis* and *S. cerevisiae*, respectively, under light and dark conditions.

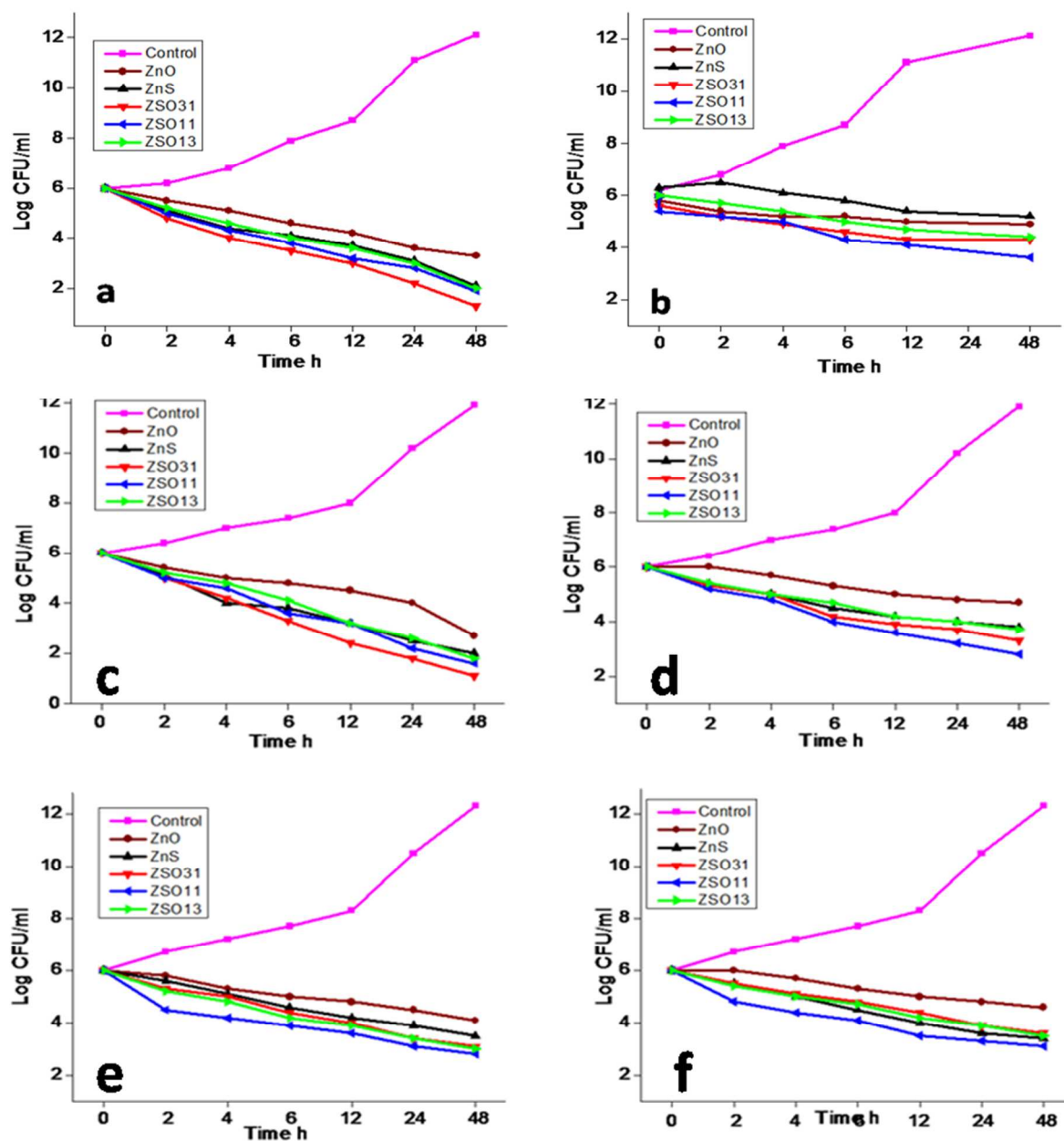


**Fig. 6** Time kill curve of *C. albicans* in (a) light and (b) dark, *C. tropicalis* in (c) light and (d) dark and *S. cerevisiae* in (e) light and (f) dark

The time-kill assay which is a measure of the rate of killing of microbes, provided a comparison of the antifungal property of the investigated samples. In the absence of nanoparticles there was an exponential growth of microbial colonies in all the investigations under light and dark conditions. It was also evident from the curves that the reduction in the growth of microbial

colonies was more pronounced in the presence of light confirming that the ROS generation by the photocatalytic nanoparticles was a dominating factor for the microbial growth resistance. On quantification, a value of  $6 \log_{10}$  (CFU/ml) at the start of experiment was found to be reduced to a value of  $1.3 \log_{10}$  (CFU/ml) for the sample ZSO31 under light. However, the same experiments under dark conditions revealed only a nominal reduction to a value of  $4.3 \log_{10}$  (CFU/ml) for ZSO31. The maximum reduction observed under dark condition was, for the sample ZSO11, to a value of  $3.5 \log_{10}$  (CFU/ml). Detailed analysis of all the three yeast species testified improved efficiency of the nanocomposites in the presence of light.

The antifungal activity observed under dark conditions was ascribed primarily due to mechanisms associated with the efflux of metal ions in solutions, as reported earlier.<sup>3, 39-41</sup> Zinc ions are known to inhibit multiple activities in the microbe cell, such as glycolysis, transmembrane proton translocation, and acid tolerance. In all the experiments, the nanocomposite particles were found to be more efficient compared to the individual particles of ZnO and ZnS. Among the three yeast species investigated, the effectiveness of nanocomposites for growth inhibition was found to be more against the *candida* species than the *S. cerevisiae*. It was also observed that though the nanocomposites were better in reducing the microbial burden, there were slight variations in the response of ZnS-ZnO compositions towards a particular yeast species. In the presence of light the efficiency of ZSO31 composition was the best for the candidal species while ZSO11 was the most effective against *S. cerevisiae*. The variation in effectiveness of the tested nanocomposites against the different yeast species was attributed to the differences in microbial cell wall structure, cell physiology, metabolism, degree of contact or surface charge of yeast cell.

### 3.3. Growth curve

The growth curves of *C. albicans*, *C. tropicalis* and *S. cerevisiae* in the presence of nanoparticles under light and dark conditions are presented in Figures 6 (a-f) respectively. The presence of nanoparticles retarded the growth of all the yeast species significantly in the presence of light and the effect was more pronounced for the nanocomposites than the individual particles of ZnO and ZnS. Among the different compositions of nanocomposites, a conclusive evidence of one efficient composition was however not obtained. Significant reduction in the growth of *C. albicans* was recorded by the combination ZSO31 and the maximum reduction was recorded between 4 and 12 h ( $p < 0.05$ ). At 48 h this combination reduced  $> 99\%$  of *Candida* species. Regrowth was not recorded for the combinations and individual components.

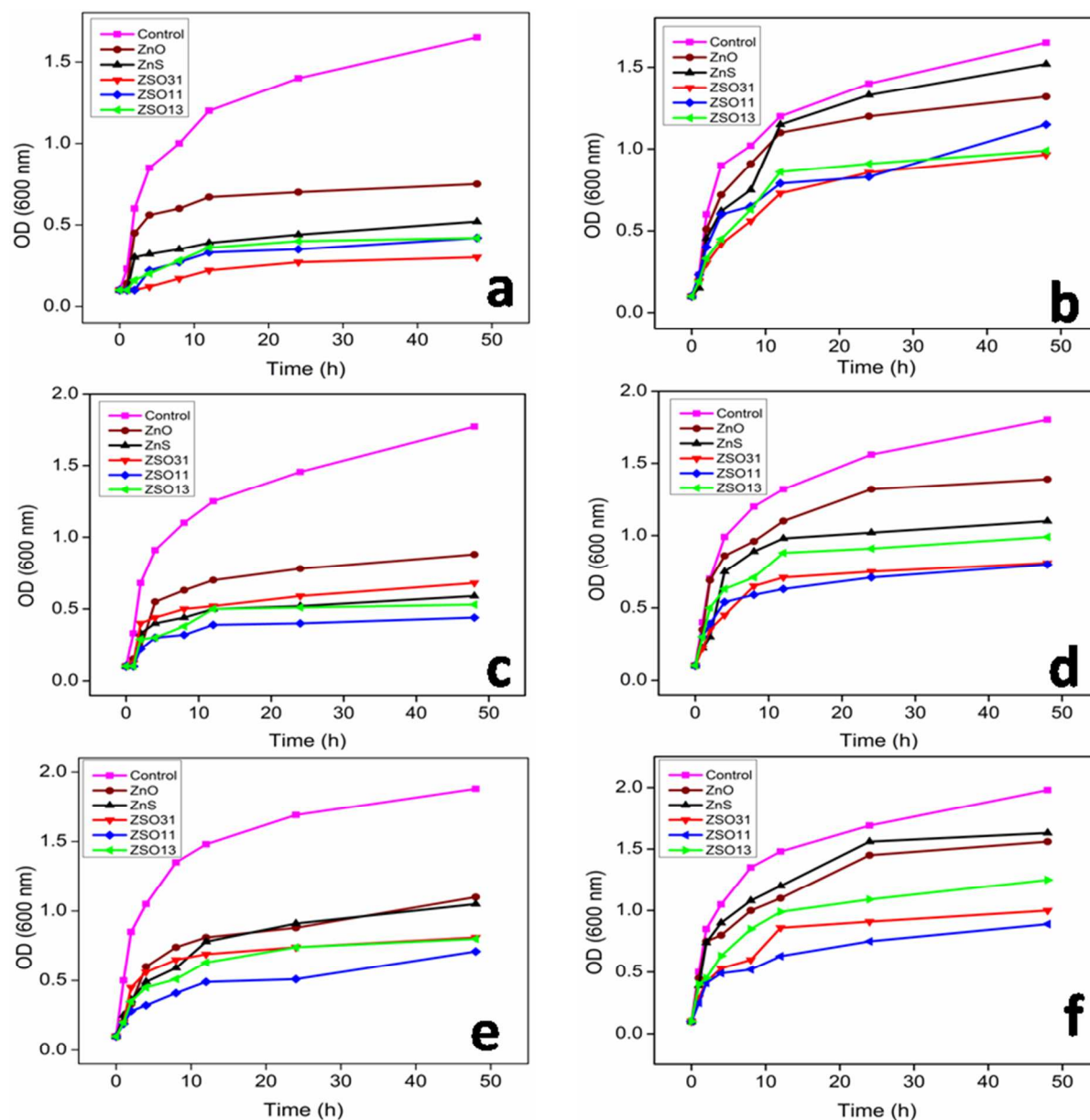


**Fig. 7** Growth curve of *C. albicans* in (a) light and (b) dark, *C. tropicalis* in (c) light and (d) dark and *S. cerevisiae* in (e) light and (f) dark

Of the three yeast species investigated, the effectiveness for growth inhibition was found to be in the order *C. albicans*>*C. tropicalis*>*S. cerevisiae*. It was also observed that there were slight variations in the response of ZnS-ZnO compositions towards a particular yeast species. Under dark conditions, the growth patterns of microbes in presence of the individual nanoparticles

closely resembled that of the control sample. The individual nanoparticles of ZnS and ZnO were found to be ineffective in growth inhibition against all the yeast species tested. The nanocomposites were relatively better though variations were observed in their effectiveness against the tested yeast species

### 3.4 Fungal membrane permeabilisation

Propidium iodide (PI), a membrane impermeable, nucleic acid staining dye, upon binding to double stranded nucleic acid gave a red fluorescence on excitation by a 480 nm laser. PI can only enter those cells, which have permeable membranes. Fungal cell membrane permeabilisation was thus studied for the nanoparticles of ZnS, ZnO and the nanocomposites of ZnO-ZnS. Since the maximum cell growth reduction was observed for *C. albicans*, PI uptake assay was monitored only for *C. albicans*. Incubation of the nanocomposite with *C. albicans* cells resulted in PI uptake by the cells as monitored by confocal microscopy (Figure 7). We observed significant increase in the PI associated fluorescence for the ZnS-ZnO nanocomposite than the individual constituents of ZnO and ZnS. This was a clear indication of increase in the membrane permeabilisation in *Candida* cells facilitated by the cell membrane rupture by ROS. No PI fluorescence was observed in control.

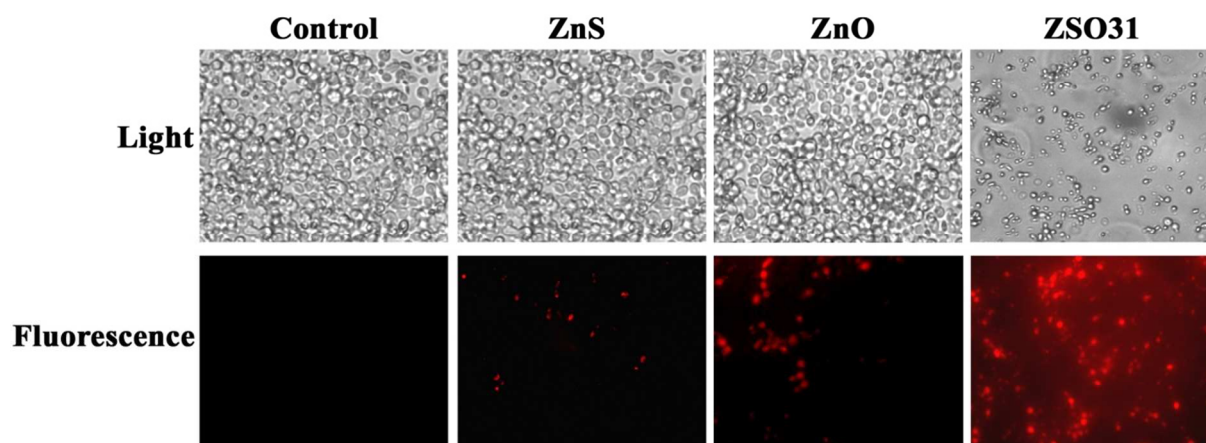


**Fig.8** Light microscope and confocal microscope images of PI stained *C. albicans* treated with ZSO31 and individual constituents

### 3.5. Role of intracellular ROS

The role of ROS generated by nanoparticles against *Candida* spp. is shown in Fig. 8. The most likely mechanism imparting antifungal activity in nanoparticles was the generation of ROS. The ZnS-ZnO nanocomposites generated more ROS than the individual nanoparticles against the tested *Candida* spp. The nanocomposite samples with 4mM histidine showed growth profile, which more or less matched that of the control sample (without nanoparticles) indicating that the generated ROS was effectively scavenged by histidine. The results thus obtained revealed that the antifungal activity of the nanoparticles is primarily related to the ROS mechanism.

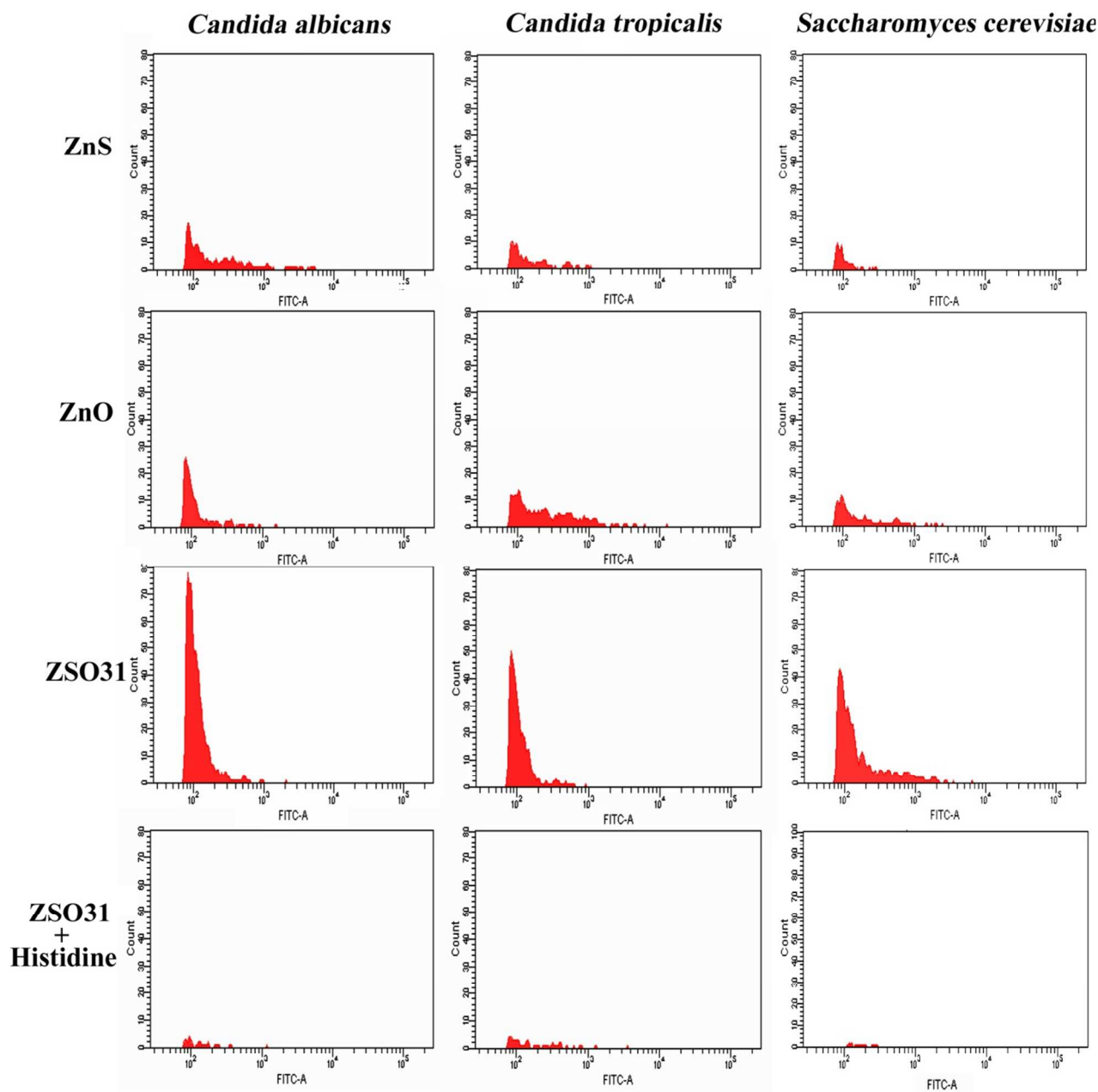


**Fig. 9** Flowcytometric Analysis on the role of ROS Formation in Yeast spp.

#### 4. Discussion

The ZnS-ZnO core shell nanocomposites obtained by the surface coverage of sub-micron sized ZnO particles by the nanoparticles of ZnS have displayed higher antifungal activity than their constituent individual particles. The red shift observed for composites towards the 400nm mark and the lowering of band gap to values less than 3eV imparted improved photocatalytic action in

the nanocomposites. The conduction band of ZnS possessed more negative potential than that of the ZnO while the valence band potential of ZnO is more positive than ZnS. The formation of ZnS-ZnO interfaces facilitated transfer of electrons from ZnS to the conduction band of ZnO and holes to the valence band of ZnS from the corresponding band of ZnO. The major factor that enabled the nanocomposite photocatalysts to out-perform their individual constituents was the enhanced charge separation achieved by tuning the energy band of ZnS with the lower potential of ZnO leading to improved efficiency through reduced recombination. The migration of charge carriers to the surfaces of ZnO and ZnS thus generated hydroxyl radical and other reactive oxygen species by reacting with moisture and oxygen. The schematic illustration of the possible mechanism is presented in Figure 9.

The antimicrobial effect of nanoparticles is ascribed primarily to the two mechanisms of ROS generation and metal ion efflux in solutions<sup>3, 42-43</sup>. The ROS generation induced cytotoxicity and caused cell decay in yeast spp. as it exceeded the antioxidative capacity of the cell. This mechanism is amply supported by literature data for a variety of nanoparticles and is comprehensively illustrated by the use of radical scavengers like histidine<sup>2, 44-45</sup>. In the present work, the antifungal activities were tested under both indoor light illumination and under dark conditions. The normal laboratory conditions involving fluorescent lighting was sufficient to generate charge carriers, leading eventually to the generation of ROS as reported earlier<sup>46</sup>. A comparative evaluation of the effectiveness of the nanocomposites under light and dark conditions revealed that the performance was better in the presence of light. The nanocomposites as well as their individual constituents displayed absorption only in the wavelengths region of 340-380 nm and hence are considered to be UV responsive only. The fact that the antimicrobial activity was best observed in the presence of light therefore suggested that the 4% UV light

fraction in indoor fluorescent lighting was sufficient to induce the required photoactivity for ROS generation, as has been observed before<sup>46</sup>. Time kill assay and growth curve analysis also suggested enhanced activity under indoor lighting than in the dark conditions substantiating the role of ROS generation by the photocatalysts. Nevertheless, the observance of greatly diminished activity under dark conditions is presumed to be due to metal ion efflux as has been proven in the case of ZnS before<sup>2</sup>. Hence the synergy of ROS and metal ion efflux is believed to be the dominant mechanism behind the enhanced antifungal activity of nanocomposite photocatalysts. The observation that the nanocomposites out-performed the individual nanoparticles in their effectiveness against all the tested yeast species confirmed the dominance of ROS over efflux mechanism. Additionally, the inhibitory role of ROS was further evidenced by the cell permeabilisation studies using propidium iodide, which resulted in enhanced fluorescence in nanocomposites compared to the individual particles of ZnO and ZnS. The increased uptake of PI into the yeast cells was a clear indication of ROS induced cell rupture as PI specifically stains only the damaged cells.

Under the same experimental conditions, the nanocomposite of ZnS-ZnO demonstrated enhanced anticandidal activity with very low MIC values than that reported previously for the individual constituents of ZnO and ZnS<sup>2, 10, 44-45, 47</sup>. The flow cytometry results confirmed the increased levels of ROS generation in ZSO31 composites against all the yeast species and were attributed to the synergistic nanocomposite effect in combination with higher surface area values (168 m<sup>2</sup>/g). It was also reported that chemisorbed OH species on ZnO surfaces in water can also lead to ROS formation<sup>48</sup>. However, in the present study none of the experimental evidences supported significant ROS generation by pure ZnO particles as they were of larger sizes and negligible surface area.

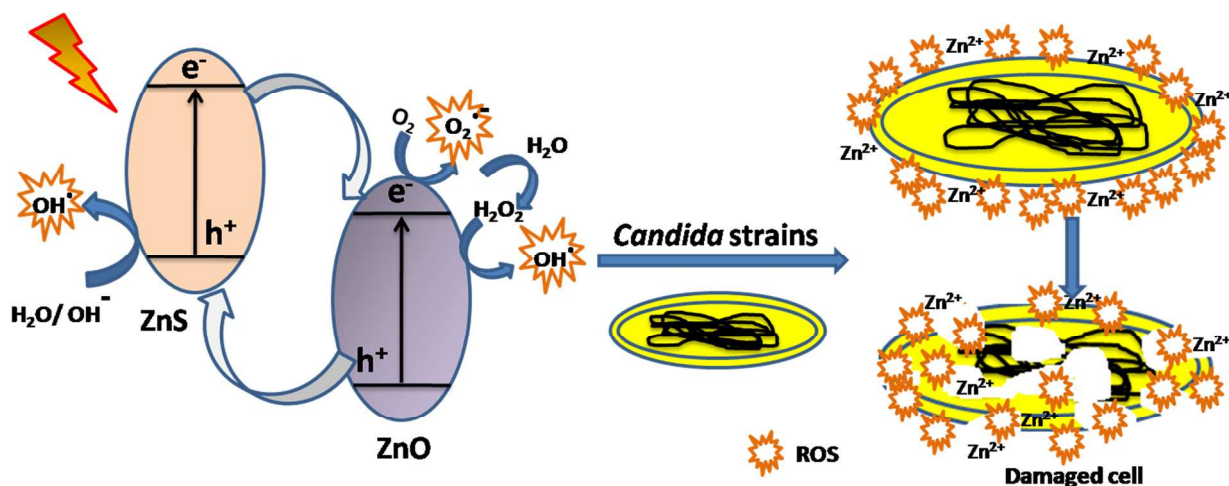


**Fig. 10** Schematic representation of band alignment leading to antifungal activity

The present study has thus led to the development of ZnS-ZnO nanocomposites with enhanced antifungal activity mediated by ROS generation under laboratory lighting conditions. The mild activity observed under dark conditions indicated the possibility of metal ion efflux also contributing to the killing of yeast cells. The synergistic effect of ZnS-ZnO nanocomposites, as illustrated schematically in Fig 9, provided enhanced charge separation leading to minimum recombination of charge carriers. This has in turn resulted in the increased effectiveness of the ZnS-ZnO nanocomposites compared to their individual constituents.

## 5. Conclusions

ZnS-ZnO nanocomposites prepared by a simple precipitation method at room temperature have displayed considerable anti-fungal activity against *C. albicans*, *C. tropicalis* and *S. cerevisiae* under normal laboratory lighting conditions. Photo induced ROS generation aided by the synergistic effects of nanocomposite architecture is the primary mechanism responsible for this enhanced performance. The inhibitory role of ROS was further confirmed by experimental

results obtained through growth curve analysis, time kill assay and cell permeabilisation studies. The studies revealed that ambient laboratory lighting conditions are conducive for the optimal performance of the nanocomposites in controlling the microbial growth of the tested yeast species. The diminished activity observed under dark conditions is ascribed to the metal ion efflux observed for zinc in solutions. The improved anticandidal activity with minimum inhibitory concentrations provides wide scope for practical applications aimed at alleviating the harmful effects of environmental contaminants.

### Acknowledgements

The authors gratefully acknowledge the Council of Scientific and Industrial Research (CSIR, Government of India) for funding the 12<sup>th</sup> five year plan project on “IntelCoat” (CSC0114). Authors P. Suyana and K. G. K. Warriar acknowledge CSIR for their fellowships. S. Nishanth Kumar thanks KSCSTE for providing a postdoctoral fellowship. Mr. Kiran Mohan, CSIR-NIIST is acknowledged for TEM Imaging.

### References

1. S. Ghosh, V. S. Goudar, K. G. Padmalekha, S. V. Bhat, S. S. Indi and H. N. Vasani, *RSC Adv.*, 2012, **2**, 930-940.
2. P. Suyana, S. N. Kumar, B. S. D. Kumar, B. N. Nair, S. C. Pillai, A. P. Mohamed, K. G. K. Warriar and U. S. Hareesh, *RSC Adv.*, 2014, **4**, 8439-8445.
3. A. S. Haja Hameed, C. Karthikeyan, S. Sasikumar, V. Senthil Kumar, S. Kumaresan and G. Ravi, *J. Mater. Chem. B*, 2013, **1**, 5950-5962.
4. G. Applerot, J. Lellouche, N. Perkas, Y. Nitzan, A. Gedanken and E. Banin, *RSC Adv.*, 2012, **2**, 2314-2321.
5. N. Perkas, A. Lipovsky, G. Amirian, Y. Nitzan and A. Gedanken, *J. Mater. Chem. B*, 2013, **1**, 5309-5316.
6. I. Perelshtein, E. Ruderman, N. Perkas, T. Tzanov, J. Beddow, E. Joyce, T. J. Mason, M. Blanes, K. Molla, A. Patlolla, A. I. Frenkel and A. Gedanken, *J. Mater. Chem. B*, 2013, **1**, 1968-1976.
7. G. Tong, F. Du, W. Wu, R. Wu, F. Liu and Y. Liang, *J. Mater. Chem. B*, 2013, **1**, 2647-2657.

8. P. K. J. Robertson, J. M. C. Robertson and D. W. Bahnemann, *J. Hazard. Mater.*, 2012, **211–212**, 161-171.
9. H. Kong, J. Song and J. Jang, *Environ. Sci. Technol.*, 2010, **44**, 5672-5676.
10. M. Fang, J.-H. Chen, X.-L. Xu, P.-H. Yang and H. F. Hildebrand, *Int. J. Antimicrob. Agents*, 2006, **27**, 513-517.
11. Q. Li, S. Mahendra, D. Y. Lyon, L. Brunet, M. V. Liga, D. Li and P. J. J. Alvarez, *Water Res*, 2008, **42**, 4591-4602.
12. C.-J. Chung, H.-I. Lin, H.-K. Tsou, Z.-Y. Shi and J.-L. He, *J. Biomed. Mater. Res. Part B Appl. Biomater.*, 2008, **85B**, 220-224.
13. C. Li, R. Younesi, Y. Cai, Y. Zhu, M. Ma and J. Zhu, *Appl. Catal. B*, 2014, **156–157**, 314-322.
14. G. Li, J. Zhai, D. Li, X. Fang, H. Jiang, Q. Dong and E. Wang, *J. Mater. Chem.*, 2010, **20**, 9215-9219.
15. Y. Li, J. Niu, W. Zhang, L. Zhang and E. Shang, *Langmuir*, 2014, **30**, 2852-2862.
16. J. Liu, L. Liu, H. Bai, Y. Wang and D. D. Sun, *Appl. Catal. B*, 2011, **106**, 76-82.
17. K. R. Raghupathi, R. T. Koodali and A. C. Manna, *Langmuir*, 2011, **27**, 4020-4028.
18. N. Cioffi, M. Rai, (Eds.), *Nano-Antimicrobials Progress and Prospects*, Springer-Verlag, Heidelberg, 1 edn, 2012.
19. J. T. Seil and T. J. Webster, *Int. J. Nanomedicine*, 2012, **7**, 2767-2781.
20. J. Zhang, Y. Wang, J. Zhang, Z. Lin, F. Huang and J. Yu, *ACS Appl. Mater. Interfaces*, 2013, **5**, 1031-1037.
21. Q. Zhao, Y. Xie, Z. Zhang and X. Bai, *Cryst. Growth Des.*, 2007, **7**, 153-158.
22. J.-S. Hu, L.-L. Ren, Y.-G. Guo, H.-P. Liang, A.-M. Cao, L.-J. Wan and C.-L. Bai, *Angew. Chem. Int. Ed.*, 2005, **44**, 1269-1273.
23. S. H. Elder, F. M. Cot, Y. Su, S. M. Heald, A. M. Tyryshkin, M. K. Bowman, Y. Gao, A. G. Joly, M. L. Balmer, A. C. Kolwaite, K. A. Magrini and D. M. Blake, *J. Am. Chem. Soc.*, 2000, **122**, 5138-5146.
24. S. K. Poznyak, D. V. Talapin and A. I. Kulak, *J. Phys. Chem. B*, 2001, **105**, 4816-4823.
25. J. Lahiri and M. Batzill, *J. Phys. Chem. C*, 2008, **112**, 4304-4307.
26. S. G. Hussain, D. Liu, X. Huang, S. Ali and M. H. Sayyad, *J. Phys. Chem. C*, 2008, **112**, 11162-11168.
27. J. Geng, B. Liu, L. Xu, F.-N. Hu and J.-J. Zhu, *Langmuir*, 2007, **23**, 10286-10293.
28. P. Chen, L. Gu and X. Cao, *CrystEngComm*, 2010, **12**, 3950-3958.
29. X. M. Shuai and W. Z. Shen, *J. Phys. Chem. C*, 2011, **115**, 6415-6422.
30. M.-Y. Lu, J. Song, M.-P. Lu, C.-Y. Lee, L.-J. Chen and Z. L. Wang, *ACS Nano*, 2009, **3**, 357-362.
31. W. Jia, B. Jia, F. Qu and X. Wu, *Dalton Trans.*, 2013, **42**, 14178-14187.
32. X. Wang, P. Gao, J. Li, C. J. Summers and Z. L. Wang, *Adv. Mater.*, 2002, **14**, 1732-1735.

33. X. Wu, P. Jiang, Y. Ding, W. Cai, S. Xie and Z. L. Wang, *Adv. Mater.*, 2007, **19**, 2319-2323.
34. L. Hu, J. Yan, M. Liao, H. Xiang, X. Gong, L. Zhang and X. Fang, *Adv. Mater.* 2012, **24**, 2305-2309.
35. X. Huang, M. Wang, M.-G. Willinger, L. Shao, D. S. Su and X.-M. Meng, *ACS Nano*, 2012, **6**, 7333-7339.
36. C. P. LeBel, H. Ischiropoulos and S. C. Bondy, *Chem. Res. Toxicol.*, 1992, **5**, 227-231.
37. D.-H. Kim, D. G. Lee, K. L. Kim and Y. Lee, *Eur. J. Biochem.*, 2001, **268**, 4449-4458.
38. I. K. Maurya, C. K. Thota, S. D. Verma, J. Sharma, M. K. Rawal, B. Ravikumar, S. Sen, N. Chauhan, A. M. Lynn, V. S. Chauhan and R. Prasad, *J. Biol. Chem.*, 2013, **288**, 16775-16787.
39. R. Brayner, R. Ferrari-Iliou, N. Brivois, S. Djediat, M. F. Benedetti and F. Fiévet, *Nano Lett.*, 2006, **6**, 866-870.
40. M. Li, L. Zhu and D. Lin, *Environ. Sci. Technol.*, 2011, **45**, 1977-1983.
41. N. M. Franklin, N. J. Rogers, S. C. Apte, G. E. Batley, G. E. Gadd and P. S. Casey, *Environ. Sci. Technol.*, 2007, **41**, 8484-8490.
42. H. Yang, C. Liu, D. Yang, H. Zhang and Z. Xi, *J. Appl. Toxicol.*, 2009, **29**, 69-78.
43. J. W. Rasmussen, E. Martinez, P. Louka and D. G. Wingett, *Exp. Opin. Drug Deliv.*, 2010, **7**, 1063-1077.
44. L. Anat, N. Yeshayahu, G. Aharon and L. Rachel, *Nanotechnology*, 2011, **22**, 105101.
45. M. Shoeb, R. S. Braj, A. K. Javed, K. Wasi, N. S. Brahma, B. S. Harikesh and H. N. Alim, *Adv. Nat. Sci.: Nanosci. Nanotechnol.*, 2013, **4**, 035015.
46. N. Jones, B. Ray, K. T. Ranjit and A. C. Manna, *FEMS Microbiol. Lett.*, 2008, **279**, 71-76.
47. Y. Wang, Q. Zhang, C.-l. Zhang and P. Li, *Food Chem.*, 2012, **132**, 419-427.
48. G. Applerot, A. Lipovsky, R. Dror, N. Perkas, Y. Nitzan, R. Lubart and A. Gedanken, *Adv. Funct. Mater.*, 2009, **19**, 842-852.